

# Connecting the Branches of Multistable Non-Euclidean Origami by Crease Stretching

Clark C. Addis, Salvador Rojas, and Andres F. Arrieta\*

*Programmable Structures Lab, School of Mechanical Engineering, Purdue University, West Lafayette, IN 47907*

(Dated: July 20, 2023)

Non-Euclidean origami is a promising technique for designing multistable deployable structures folded from nonplanar developable surfaces. The impossibility of flat foldability inherent to non-Euclidean origami results in two disconnected solution branches each with the same angular deficiency but opposite handedness. We show that these regions can be connected via “crease stretching” wherein the creases exhibit extensibility in addition to torsional stiffness. We further reveal that crease stretching acts as an energy storage method capable of passive deployment and control. Specifically, we show that in a Miura-Ori system with a single stretchable crease, this is achieved via two unique, easy to realize, equilibrium folding pathways for a certain wide set of parameters. In particular, we demonstrate that this connection mostly preserves the stable states of the non-Euclidean system, while resulting a third stable state enabled only by the interaction of crease torsion and stretching. Finally, we show that this simplified model can be used as an efficient and robust tool for inverse design of multistable origami based on closed-form predictions that yield the system parameters required to attain multiple, desired stable shapes. This facilitates the implementation of multistable origami for applications in architecture materials, robotics, and deployable structures.

## I. INTRODUCTION

Origami is the ancient Japanese art of paper folding. The simple algebraic kinematics of origami-inspired systems gives rise to its characteristic reconfigurability, which has resulted in numerous applications, in robotic locomotion [1–4], metamaterial architecture [5], compact deployable structures such as bridges and stadium covers [6], reconfigurable wheels [7], and – notably – simple yet robust inverse shape design algorithms [8–11]. Classical origami assumes that shape change stems from folding of an infinitely thin surface involving no deformation or change in strain energy [12]. Consequently, engineering systems inspired by origami formalism theoretically behave as mechanisms, which by definition do not resist displacement along their degrees of freedom. However, physical embodiments of origami [13] do in fact show resistance to displacement, either due to torsional stiffness [14], or active elements used to achieve desired kinematic configurations [15]. The former typically shows a single stable shape, while the latter can achieve several configurations at the cost of complex actuation systems and control.

Engineers have investigated the potential of origami with multiple energetic minima, or multistable origami, to add load bearing capacity and pathway configurability without the need for continuous actuation and complex control. One approach takes advantage of hidden degrees of freedom due to facet bending [16–19]. However, this excludes the utilization of functional materials such as semiconductors (e.g. photovoltaics or transistors) that cannot cope with the large facet strains experienced during bending.

A second approach assumes rigid facets instead relying on elastic bending moments via crease torsion to produce

multistability [20–22]. Waitukaitis et al. have shown that crease torsion alone can achieve up to five stable configurations for a 4-facet origami system [23]. However, two key drawbacks remain: (1) the folding paths have multiple solutions which overlap at the flat state [24], and (2) inverse design is difficult due to the coexisting solutions (pathway degeneracy) and the complex multidimensional problem of fine tuning the crease stiffness to match a desired state [25–27].

Non-Euclidean origami shows promise to address some of these challenges. This class of origami is still folded from developable, zero Gaussian curvature sheets, but instead of subtending an angle of  $2\pi$  about a particular vertex, as is the case for traditional origami, it is folded from some angular deficiency of less than  $2\pi$  (a cone [28, 29]) or some angular excess of greater than  $2\pi$  (an E-cone [30]). Non-Euclidean origami circumvents the pathway degeneracy of traditional origami because it will always result in two separate folding regimes when folded from a cone no matter how many creases are added [28, 31]. Intuitively, this is because the two regions represent two mirrored cones [Figure 1 (a)]. The kinematics of non-Euclidean origami preserve the ability to be described by simple algebraic equations [32–34], and in many instances has succeeded in passively prevent misfolding [29, 35, 36]. This comes at the cost of effectively halving the possible design space.

Resilin, a multipurpose biopolymer commonly found in insect wings [37–40] serves as an inspiration to expand this design space while enabling multistability. Resilin assigns mountain or valley folds to origami-like insect wings [41, 42] and serves as an energy storage device, for example in the Rove Beetle [43] and the Earwig [44]. However, the Earwig wing is unique in that the energy is stored via stretching in the creases in addition to crease torsion. This crease stretching or “spring origami” has been shown to explain the bistability and curved creases displayed by the Earwig wing [45], opening up a vast de-

---

\* aarrieta@purdue.edu

sign space for origami-based systems which localizing all flexibility to the folds.

In this paper, we show that crease stretching can connect the oppositely handed folding regimes of non-Euclidean origami without relying on facet deformation, while retaining the benefit of simple pathway control and straightforward inverse design. This is achieved by establishing a tractable analytical method applied to the well known Miura-Ori unit. We begin with the Miura-Ori folded from the two possible non-Euclidean cones, then relax the rigid crease assumption of classical origami by allowing them to stretch while maintaining infinite facet rigidity. By folding the manifold representing the kinematic space into the energetic space, we can show that inherent symmetries directly predict the existence of a minimum of two, and usually three stable configurations. Furthermore, through derivation of the folding paths, our model allows us to show that crease stretching does not add degeneracy. The analytically predicted configurations and folding paths accurately match benchtop experiments. Our results show that the stable states from the purely non-Euclidean approach are mostly preserved, while adding a third. Finally, we show how the model is simple enough to be used in inverse design calculations, yet robust enough to be confirmed by experiments.

## II. ALTERNATIVE MODELS FOR CREASE STRETCHING

We begin with a discussion of alternative models of flexible creases in origami. For sufficiently thin sheets, a straightforward approach is to neglect the effect of stretching, and to assume that the energetics of crease bending are dominated by torsional deformations. Models based on symmetric Elastica curves make use of rotational springs at curve intersection [46–49], while others ignore the bulk and focus on a single nonlinear [50, 51] or linear [52–56] spring whose constants are based on material models. However, we cannot discount crease extensibility during bending because (1) we employ thick creases in this work as thin creases are difficult to manufacture using fused deposition modelling (FDM) 3D printing and (2) we know that kinematically the angular material must be able to stretch to accommodate the transition between non-Euclidean cones. A second approach is to create beam-like models which has been achieved using finite element methods [57–59], or hyperelastic material models [60]. While highly descriptive and accurate, these beam-like models are computationally expensive and difficult to perform inverse on.

The F-cone model which entails a cone with at least one fold in it [61] is the closest analytical model that can account for both torsion and stretching. Notably, F-cones remains bistable, even when part of the central fold is removed [62], a fact that we leverage in our experiments. Nevertheless, the deformation process is still rather complex to model, requiring numerical approximations [63],

which makes this approach cumbersome for inverse design.

“Spring origami” offers a computationally simple yet powerful model where the crease is represented by a combination of a rotational and extensional spring [45]. Rojas et al. have used it to model 3D printable multistable grippers [64] and the reconfiguration of temperature sensitive shape memory polymers [65]. Due to its ability to capture both the torsion and stretching of a system with the minimum possible complexity, we choose to use “spring origami” throughout this work.

## III. PROBLEM DEFINITION

Non-Euclidean origami refers to a 2D surface with sector angles  $\rho_i$  subtending an angle of  $2\pi + \epsilon$  about the vertex [29], where  $\epsilon$  is the angular excess. Equivalently, the surface can be folded from sectors with a subtending angle of  $2\pi - \beta$  [45], where  $\beta$  is the angular deficit. In general,  $\beta = -\epsilon$ , and we will use  $\beta$  throughout, since pathway disconnection occurs only in systems with angular deficit [28]. We choose to examine a Miura-Ori unit, an origami fold pattern originally developed for folding membranes in space mechanisms [66], given the extensive attention it has received in the literature and its univer-

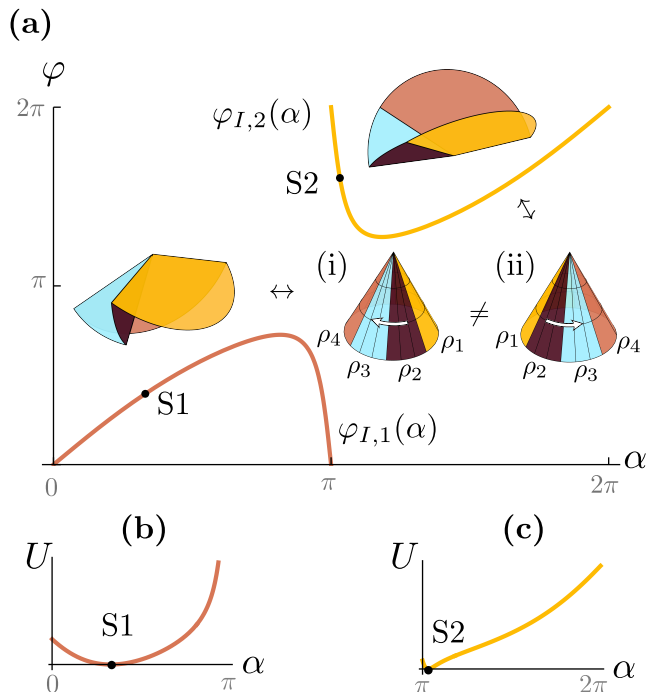


FIG. 1. (a): Non-Euclidean origami with an angular deficiency has two disconnected pathways, each represented by an oppositely handed cone. When a rotational spring is added, two disconnected stable states form (b): The energy landscape for path/cone 1 and stable state S1 (c): The energy landscape for path/cone 2 and state S2.

sal applications. For a symmetric Miura-Ori unit, one additional geometric parameter  $\gamma$  [5] is required to define the symmetric facets  $\rho_1 = \rho_4$  [shown in Figure 1 (a) (i)]. Using spherical trigonometry for the basic case of a non-Euclidean system without crease stretching we can write the kinematics (see derivation details in SI A.3.5) as:

$$\varphi_{I,n}(\alpha) = 2 \tan^{-1} \left[ \frac{\sin \alpha}{-\cot(\gamma + \beta/2) \sin \gamma - \cos \gamma \cos \alpha} \right] + 2\pi(n-1), \quad (1)$$

with  $n = 1$  or  $n = 2$ , where  $\varphi$  and  $\alpha$  are the dihedral angles defined in Figure 3 (a). Notice, that Eq. (1) results in two folding pathways:  $\varphi_{I,1}(\alpha)$  (left) and  $\varphi_{I,2}(\alpha)$  (right), plotted in Figure 1a (a) as Eq. (1) with  $\gamma = 3\pi/4$ , and  $\beta = 10^\circ$ . This matches prior work establishing that for  $\beta > 0$  two disconnected pathways always exist [28]. The disconnected pathways can be abstracted as two “oppositely handed” cones. For path 1, when viewed with the vertex at the top,  $\rho_i$  cyclically increases in the clockwise direction around the directrix [Figure 1 (a) (i)], whereas for path 2,  $\rho_i$  cyclically increases in the counterclockwise direction around the directrix [Figure 1 (a) (ii)].

We consider the addition of a rotational spring between facets  $\rho_2$  and  $\rho_3$ , with an equilibrium angle  $\theta_0 = 79.76^\circ$  which reveals two stable states S1 and S2. The equilibrium angle  $\alpha_{0,1}$  for stable state S1 on pathway 1 can be calculated using:

$$\alpha_{0,1} = \cos^{-1} \left[ \frac{\cot \gamma \sin \eta}{\sqrt{\cos^2 \eta + \cot^2(\theta_0/2)}} \right] - \tan^{-1} \left[ \frac{\cot(\theta_0/2)}{\cos \eta} \right], \quad (2)$$

and the equilibrium angle  $\alpha_{0,2}$  for stable state S2 on pathway 2 can be calculated as:

$$\alpha_{0,2} = 2\pi - \cos^{-1} \left[ \frac{\cot \gamma \sin \eta}{\sqrt{\cos^2 \eta + \cot^2(\theta_0/2)}} \right] - \tan^{-1} \left[ \frac{\cot(\theta_0/2)}{\cos \eta} \right]. \quad (3)$$

Eqs. (2) and (3) are derived by using spherical trigonometry and the harmonic identity to locate the coordinates where the gradient of the energy is zero as detailed in SI B.3. Notice, however, that in Figures 1 (b) and (c) the two stable states lie on two different pathways. Thus, these two stable states could never be physically realized on the same rigid system. These disconnected pathways (i.e., disjointed sets) are an intrinsic characteristic of n-fold, non-Euclidean origami with an angular deficiency [28]. In the following, we establish a

method to connect these disjointed regions in a physical system while retaining bistability by allowing crease stretching.

#### IV. PARAMETER SPACE

We first define the derived parameter  $\eta$ , which is equivalently the facet angle subtending  $\rho_2$ , and the facet angle subtending  $\rho_3$  [Figure 2 (a)]. We define that in the flat state,  $\eta$ ,  $\gamma$ , and  $\beta$  lie in a plane [see Figure 2 (b) for definition of  $\gamma$  and  $\beta$  and Figure 2 (c) for definition of  $\eta$ ]. Thus, they are explicitly related by:

$$2\eta + 2\gamma + \beta = 2\pi. \quad (4)$$

We introduce parametric bounds on our system, by first enforcing that  $\eta > 0$ , implying that facets  $\rho_2$  and  $\rho_3$  will always exist. Using Eq. (4), this definition is equivalent to the statement:

$$\gamma < \pi - \beta/2. \quad (5)$$

To allow for the space folding technique employed in section VI, we impose that the kinematic space always form a closed region using the two kinematic boundaries we establish in section V (see SI A.4.1 for details) resulting in the additional restriction that:

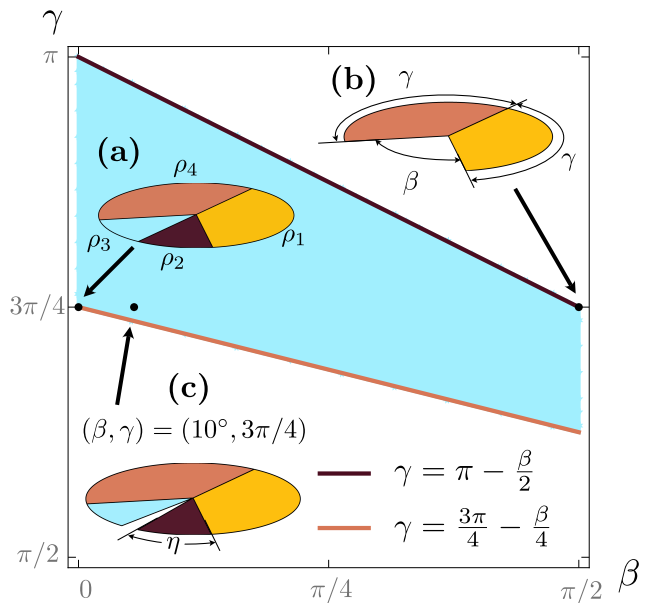


FIG. 2. The valid parameter space for this analysis is highlighted by the shaded area. There are two boundaries: the upper boundary corresponds to  $\eta = 0$ , and the lower boundary simplifies the kinematic analysis. The point at  $\beta = 10^\circ$  and  $\gamma = \frac{3\pi}{4}$  is used throughout this study.

$$\gamma > 3\pi/4 - \beta/4. \quad (6)$$

Finally, to further simplify our analysis (see SI A.3.3 for full justification), we restrict  $\beta$  and  $\gamma$  to the domains:

$$0 < \beta < \pi/2 \quad \text{and} \quad \pi/2 < \gamma < \pi. \quad (7)$$

The four constraints given by Eqs. (5-7) form a closed region represented by the shaded area in Figure 2. The geometric parameters used throughout this article are  $\beta = 10^\circ$  and  $\gamma = 3\pi/4$  [Figure 2 (c)].

## V. KINEMATICS AND ENERGETICS

The kinematic analysis of a stretchable crease unit requires the definition of two independent degrees of freedom  $\varphi$  and  $\alpha$  [Figure 3(a)]. This effectively creates a cut at  $\rho_2$  and  $\rho_3$ . Allowing  $\varphi$  and  $\alpha$  to both be members of the open set  $(0, 2\pi)$  provides all possible configurations of the system.

To represent a flexible crease [the material between  $\rho_2$  and  $\rho_3$  in Figure 3 (a)], we use a rotational spring of stiffness  $k_T$  with equilibrium angle  $\theta_0$  and an extensional spring of stiffness  $k_E$  with equilibrium distance  $x_0$  [Figure 3 (b)], which act on  $\theta$  and  $x$  respectively [Figure 3 (c)]. We define  $\theta$  to be the angle subtended by the spherical arc  $CD$  from point F, while we define  $x$  as the Euclidean distance between points C and D. Finally, we assume the restoring force from the stretchable crease to be of a significantly higher order of magnitude than the potential due to gravity allowing us to ignore the effect of mass in the facets ( $\rho_i$ ). The resulting energetics are captured by:

$$U = \frac{1}{2} (k_E[x(\alpha, \varphi) - x_0]^2 + k_T[\theta(\alpha, \varphi) - \theta_0]^2). \quad (8)$$

Interestingly, assuming rigid facets and lumped springs impose two kinematic constraints on the system. These two constraints can be described by the parameter  $g = FC = FD$  [Figure 3 (c)]. The first constraint is that facets  $\rho_2$  and  $\rho_3$  cannot intersect, corresponding to  $x = 0$ , or  $g = 0$  in Figure 3 (d). Equivalently, this boundary is the kinematic space of a non-Euclidean system without crease stretching, and thus is directly defined by Eq. (1). We refer to this as the ‘‘intersect boundary,’’  $\varphi_I$ . The second constraint is  $g = \pi/2$ , which corresponds to when facets  $\rho_2$  and  $\rho_3$  are parallel to each other, rendering impossible the placement of a rotational spring. We refer to this as  $\varphi_S$ , for ‘‘spring boundary,’’ and it is defined by (see SI A.3.4 for this derivation):

$$\varphi_S(\alpha) = \pi - 2 \tan^{-1} \left( \frac{\tan(\gamma + \beta/2) \sin \gamma - \cos \gamma \cos \alpha}{\sin \alpha} \right). \quad (9)$$

We plot Eqs. (1) and (9) in  $\alpha - \varphi$  space [Figure 3 (d)] and show that they always form a closed region, given the parameter limits outlined in Figure 2 (see SI A.4 for details).

## VI. STABILITY ANALYSIS

Transforming the kinematics from  $\alpha - \varphi$  to  $x - \theta$  coordinates simplifies the stability analysis because the energetics of the problem, as defined in Eq. (8), are in  $x$  and  $\theta$ . However,  $x - \theta$  coordinates do not provide a one-to-one mapping to  $\alpha - \varphi$  coordinates as described in SI A.5. This motivates our choices to use  $x - \theta - \varphi$  coordinates to represent the system, which effectively folds  $\alpha - \varphi$  space into 3 dimensions, as shown in Figure 3 (e), and provides a one-to-one mapping to  $\alpha - \varphi$  space. To characterize this surface, we can write a level curve  $f(x, \theta, \varphi) = 0$ , using the spherical law of sines, as detailed in SI A.7, yielding:

$$f(x, \theta, \varphi) = \frac{\sin(\theta/2)}{\sin \gamma} - \frac{\sin(\varphi/2)}{\sin \left( \eta + \sin^{-1} \left[ \frac{x}{2 \sin(\theta/2)} \right] \right)} = 0. \quad (10)$$

Prior work has established that energy minima, and thus stable states, occur when the gradient of energy ( $\nabla U$ ) and the gradient of the kinematic space ( $\nabla f$ ) point in the same direction [67]. Using the dot product, this statement can be equivalently written as:

$$\nabla U \cdot \nabla f = |\nabla U| |\nabla f|, \quad (11)$$

where the gradient operator is defined in  $x - \theta - \varphi$  coordinates. Applying this definition of the gradient to Eq. (8) and Eq. (10), yields  $\nabla f$  and  $\nabla U$  as:

$$\nabla U = [k_E(x - x_0), k_T(\theta - \theta_0), 0] \quad (12)$$

and

$$\nabla f = \left[ \frac{\partial f}{\partial x}, \frac{\partial f}{\partial \theta}, \frac{\partial f}{\partial \varphi} \right]. \quad (13)$$

Notice that Eq. (12) establishes that the energy gradient is always a 2D vector, and Eq. (13) reveals that kinematic gradient is in general a 3D vector. Therefore, the two vectors point in the same direction only when the kinematic vector degenerates into a 2D vector in the  $x - \theta$  plane. Inspection of Eq. (13) reveals that this collapse occurs when  $\partial f / \partial \varphi = 0$ . Our analysis in SI B.1.2 shows that  $\partial f / \partial \varphi = 0$  occurs when  $\varphi = \pi$ . We can visually establish in Figure 4 (a) that this stable state (T3) indeed occurs within the plane  $\varphi = \pi$  in  $x - \theta - \varphi$  space, and in Figure 4 (b) on the line  $\varphi = \pi$  in  $\alpha - \varphi$  space.

To uncover the other stable states, we re-examine Eq. (11) and determine that  $\nabla f = 0$  or  $\nabla U = 0$  also satisfy

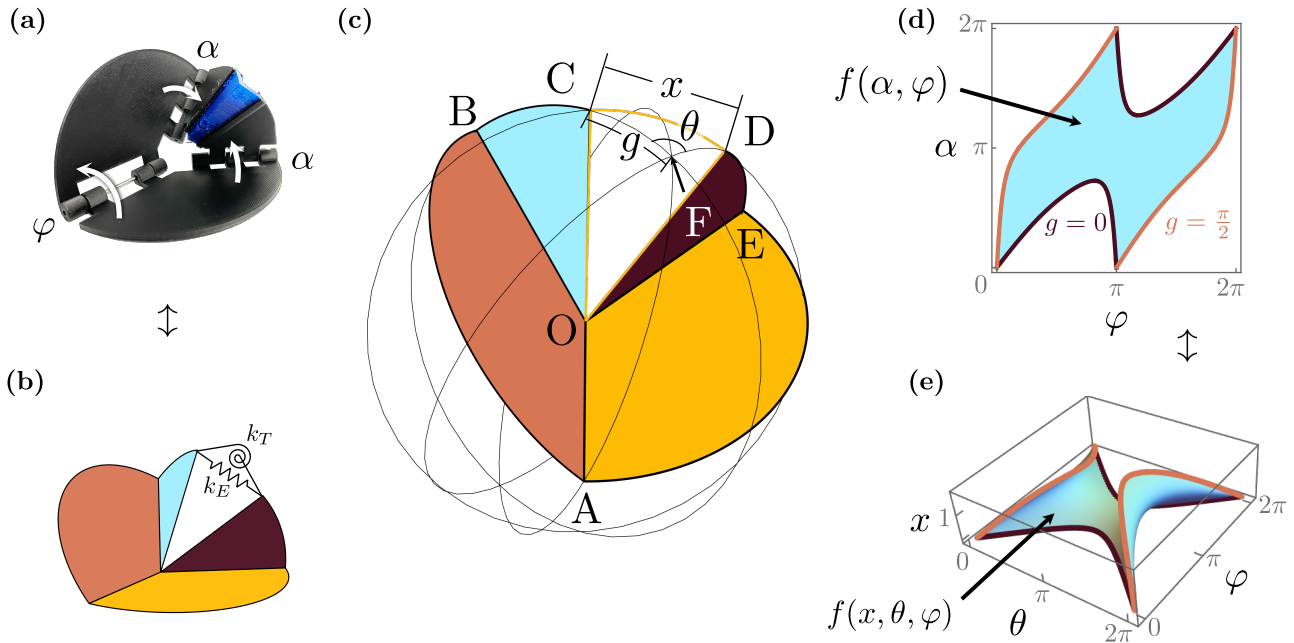


FIG. 3. (a): We treat the stretchable crease as a torsional and extensional spring with stiffness  $k_T$  and  $k_E$  (b): The 2 degrees of freedom,  $\varphi$  and  $\alpha$  completely define the kinematic space (c): If all of the dihedral edges are unit length, all endpoints lie on a sphere. The spring  $k_E$  acts over distance  $x$ , which is the chord from point C to point D, and the spring  $k_T$  acts about angle  $\theta$  which is the angle defined by  $\triangle CFD$  about point F. The parameter  $g$  is useful in establishing the kinematic bounds, and it is equal to arc  $FC = FD$  (d): Not all  $\varphi - \alpha$  pairs are valid. When  $g = 0$  the facets intersect, and when  $g = \pi/2$  the extensional spring clips through the facets, both of which are physically impossible (e): We can fold the  $\alpha - \varphi$  kinematic space into  $x - \theta - \varphi$  space to simplify the energetic analysis.

this expression. We show in SI B.1.3 that  $\nabla f$  is never zero and from inspection of Eq. (12) we observe that  $\nabla U = 0$  when  $x = x_0$  and  $\theta = \theta_0$ . This result implies that additional stable states appear according to the number of  $(\alpha, \varphi)$  pairs that can produce a specific  $(x, \theta)$  pair. Specifically, we reveal in SI A.5 that every  $(x, \theta)$  pair, corresponds to two  $(\alpha, \varphi)$  pairs, with the notable exception at  $\varphi = \pi$ , i.e., the flat folded configuration. Figure 4 (a) reveals a visual intuition for why this is true: the solid line, which represents a given  $(x_0, \theta_0)$ , intersects the surface  $f$  twice, at T1 and T2 and is symmetric about  $\varphi = \pi$ . The equations used to obtain  $(\alpha_1, \varphi_1)$  and  $(\alpha_2, \varphi_2)$  for T1 and T2 respectively, are derived using Napier's analogies and the spherical law of sines in SI A.5, which yields the following conditions:

$$\varphi_1 = 2 \sin^{-1} \left[ \frac{\sin \frac{\theta_0}{2}}{\sin \gamma} \sin \left( \eta + \sin^{-1} \left[ \frac{x_0}{2 \sin \frac{\theta_0}{2}} \right] \right) \right], \quad (14)$$

and

$$\varphi_2 = 2\pi - \varphi_1, \quad (15)$$

with

$$\alpha_{1,2} = 2 \tan^{-1} \left[ -\frac{\cos \left( \frac{1}{2}[\gamma \pm \eta] \right)}{\cos \left( \frac{1}{2}[\gamma \mp \eta] \right)} \tan \left( \frac{\varphi_1}{4} - \frac{\theta_0}{4} \right) \right]. \quad (16)$$

To obtain state T3, we write  $U$  as a function of  $\alpha$ , holding  $\varphi$  constant at  $\pi$  and setting  $\partial U / \partial \alpha = 0$  (SI B2). Note that this requires choosing a ratio of  $k_E / k_T$ . We chose  $10^3$  because it is close to the range considered in Ref. [45] for which the predictions obtained with our model reveal the parameter values for the three stable states, as summarized in Table I.

The predicted parameter values by our closed-form solutions enable the design of the experimental demonstrator shown in Figure 4 (b). In this demonstrator, we observe the symmetry of states T1 and T2 about  $\varphi = \pi$  which have identical  $(x, \theta)$  values. Additionally, the third stable state (T3), is found at  $\varphi = \pi$ . These experimental observations match closely the theoretical model predictions in Table I.

We now compare the stable states found by strict non-Euclidean origami [Figure 1 (a)] to the stable states for an equivalent system with the addition of crease stretching [Figure 4 (c)]. Note that the shaded region in Figure 4 (c) represents the kinematic space for crease stretching whereas the solid lines represents the kinematic space of

strict non-Euclidean origami. Without crease stretching, we observe two disconnected stable states, S1 and S2. In contrast, allowing the crease to stretch connects the states via the shaded region (T1 and T2) and introduces an additional, kinematically accessible, third stable state (T3). Consequently, crease stretching connects the otherwise disjointed two stable states, i.e., S1 and S2.

## VII. FOLDING PATHWAYS

Figure 4 (b) showed that the three stable states have no kinematic obstacles between them. Here, we elucidate the two equilibrium folding pathways by which these states are connected using the Principle of Virtual Work (SI C). This approach reveals that there are two possible equilibrium pathways, one for each degree of freedom. One pathway corresponds to  $\frac{\partial U}{\partial \alpha} = 0$ . A solution to this equation fixes points O and A and applies two vertical downward forces,  $F_\alpha$ , at B and E [Figure 5 (a) (i)]. We define this to be the  $\varphi$ -path because  $\varphi$  is our degree of freedom. The energy along this pathway is shown in Figure 5 (b). Notice that the endpoints of this path are T1 and T2, the two stable states established earlier. The

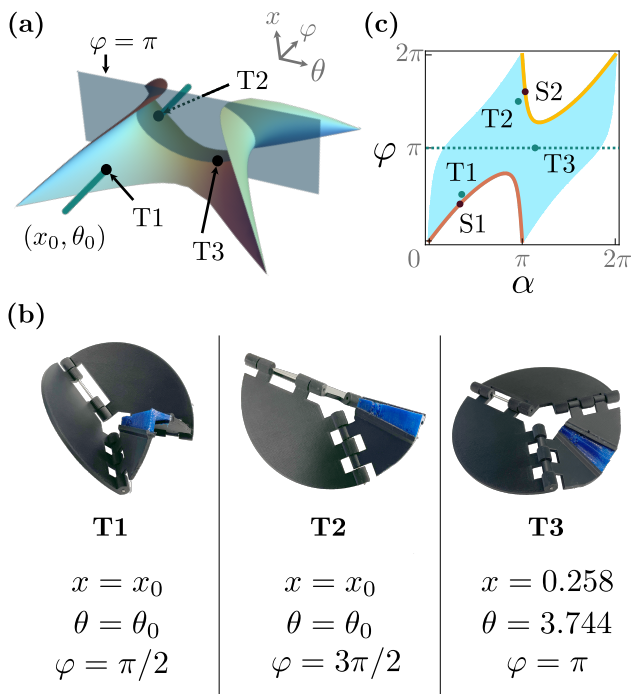


FIG. 4. (a): Our model predicts 3 stable states, two of which result from the global minimum (T1, T2) and one which is a local minimum of the balance of crease torsion and stretching (T3). (b): We can see visually that the global minimum of  $x_0$  and  $\theta_0$  occurs twice (T1, T2). We can show mathematically that the global minimum can only occur along the plane  $\varphi = \pi$  (T3). (c): This model is verified by experiments.

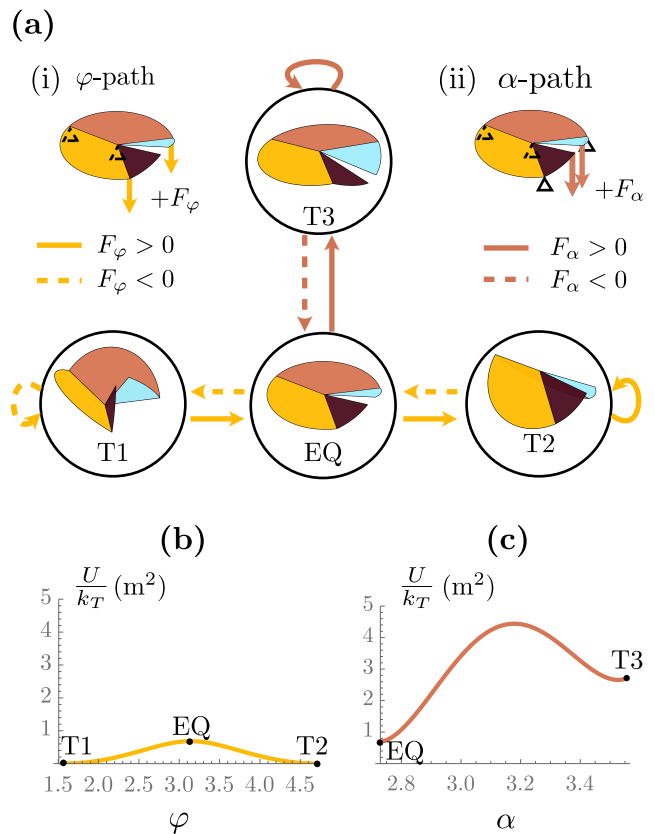


FIG. 5. (a): Stable states T1, T2, and T3 are connected by two main pathways (i) the  $\varphi$ -path where  $\varphi$  is the only DOF, where when a  $+F_\varphi$  is applied results in system folding from T1 to EQ and EQ to T2, and (ii) the  $\alpha$ -path where  $\alpha$  is the only DOF, which when a positive  $F_\alpha$  is applied results in folding from EQ to T3 (b): Energy landscape along the  $\varphi$ -path, showing local maximum at EQ and local minima at T1 and T2 (c): the energy landscape along the  $\alpha$ -path, showing local minima at EQ and T3.

other path corresponds to  $\frac{\partial U}{\partial \varphi} = 0$ . This pathway requires fixing points O, A, B, and E, and applying two vertical forces  $F_\alpha$  at C and D, see Figure 3 (c) for the definition of points A-E and O. We define this to be the  $\alpha$ -path [Figure 5 (a) (ii)] because  $\alpha$  is our degree of freedom. The energy along this pathway is shown in Figure 5 (c). The full energy landscape for the entire kinematic space is shown in Figure 6 (a).

TABLE I. Degrees of freedom values and stability conditions predicted by our model for the three stable states for a system with parameters  $\gamma = 3\pi/4$ ,  $\beta = 10^\circ$ ,  $x_0 = 0.25$ ,  $\theta_0 = 1.39$ , and  $k_E/k_T = 10^3$ .

State	$x$	$\theta$	$\alpha$	$\varphi$	$\nabla U, \nabla f$
T1	0.250	1.39	1.10	$\pi/2$	$\nabla U = 0$
T2	0.250	1.39	3.01	$3\pi/2$	$\nabla U = 0$
T3	0.258	3.74	3.57	$\pi$	$\nabla U /  \nabla U  = \nabla f /  \nabla f $

Notice that in Figure 5 (c), state T3 is not connected directly to states T1 or T2. Instead, its endpoint is an intermediate saddle point EQ. Figure 5 (a) summarizes how T1, T2, T3, and EQ are connected by the  $\alpha$  path and the  $\varphi$  path. For instance, if we desire to move from state T1 to state T2, we would apply a positive  $F_\varphi$  to the system with the boundary conditions of the  $\varphi$ -path. Application of a positive  $F_\varphi$  past state T2, results in deflection back to state S2 upon release (See Video S1). Figure 5 (a) also indicates that to access state T3 from T1 requires the application of a positive  $F_\varphi$  under the boundary conditions of the  $\varphi$ -path until the system is at the saddle point, EQ. Then, by switching a positive  $F_\alpha$  with the boundary conditions of the  $\alpha$ -pathway, the system reaches state T3. Continuing to apply a positive  $F_\alpha$  and subsequent release results in self-equilibrating deflection into state T3 (See video S2). For a given transition from one state to another, Figure 5 (c) can be read by starting at the initial state, and then applying  $\pm F_\alpha$  or  $\pm F_\varphi$  until the desired final state is reached.

### VIII. INVERSE DESIGN

We now shift to the ultimate focus of this paper: to inversely design a spring origami Miura-Ori unit. We begin with a justification of our choice of design objective. Since there are a small number of elastomeric materials available for our manufacturing process (FDM 3D printing), we relate  $k_E$  and  $k_T$  at a ratio of  $k_E/k_T = 10^3$ , as before. We have also shown that choosing the shape of either T1 or T2 [ $(\varphi_{T1}, \alpha_{T1})$  or  $(\varphi_{T2}, \alpha_{T2})$ ] implies defining the other state's shape given their  $2\pi$  symmetry in  $\varphi$

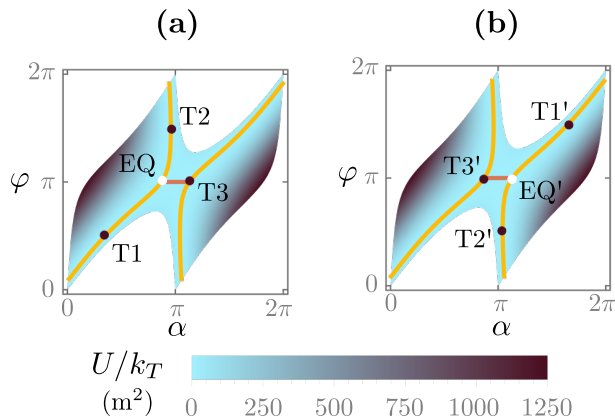


FIG. 6. Folding pathways, resulting stable states, and normalized strain energy choosing  $\varphi_{0,1}$  (value of  $\varphi$  at T1) and  $x_0$  as design objectives and  $\theta_0$  as our design variable. (a) For the design objective of  $\varphi_{0,1} = \pi/2$  and  $x_0 = 0.25$  inverse design results in  $\theta_0 = 1.39$  (b) The same design objective is also achieved using  $\theta_0 = 2\pi - 1.39$ . By choosing one (a) or (b), we can control whether the two stable states have  $\alpha$  values in the open interval (a):  $(0, \pi)$  or (b):  $(\pi, 2\pi)$ .

[see Eq. (15) and Eq. (16)]. Therefore, the full range of available design variables are:

$$\gamma, \beta, x_0, \theta_0, \quad \text{and} \quad (\varphi_{T1}|\varphi_{T2}|\alpha_{T1}|\alpha_{T2}) \quad (17)$$

To perform inverse design, we can now choose any four variables from Eq. 17 and determine the fifth. We illustrated this process, fixing  $\gamma$ ,  $\beta$ ,  $x_0$ , and  $\varphi_{T1}$  and calculating the required  $\theta_0$ . To simplify our kinematics, we keep the parameters fixed at  $\gamma = 3\pi/4$  and  $\beta = 10^\circ$  as in Figure 2 (c). We select  $\varphi$  as our design objective over  $\alpha$  since all of its facets are connected to standard origami linkages, so linking the units kinematically to an origami string [68], or an origami metamaterial [5] would be a simple task. We choose  $x_0$  as the second design objective, as limitations from the herein employed fabrication method, imposes restrictions on manufacturing larger  $x_0$  values. However, freer choice of manufacturing processes would allow for the selection of  $\theta_0$  as design objective. To illustrate this process, we explicitly derive the  $\theta_0$  required to achieve a given  $\varphi_{0,1}$ - $x_0$  pair, as detailed in SI A.8, yielding:

$$\theta_0(x_0, \varphi_{0,1}) = 2 \sin^{-1} \left( \frac{x_0 \sqrt{A^2 + 1}}{2A} \right) \quad (18a)$$

or

$$2\pi - 2 \sin^{-1} \left( \frac{x_0 \sqrt{A^2 + 1}}{2A} \right) \quad (18b)$$

where

$$A = \frac{\sin \eta}{\frac{2}{x_0} \sin \frac{\varphi_{0,1}}{2} \sin \gamma - \cos \eta}. \quad (19)$$

Notice that Eq. (18) reveals there are two possible  $\theta_0$  values that satisfy our desired  $\varphi_{0,1}$  and  $x_0$ , where the first applies for  $\theta_0 \in (0, \pi)$  and the second for  $\theta_0 \in (\pi, 2\pi)$ .

To understand the difference between these two values of  $\theta_0$ , we choose a representative design point of  $\varphi_{0,1} = \pi/2$  and  $x = 0.25$  for simplicity. Using Eq. (18a) we obtain the value  $\theta_0 = 1.39$ , and using Eq. (18b) we obtain the value  $\theta_0 = 2\pi - 1.39$ , both of which satisfy our design requirement. Figure 6 (a) shows what the stable states and the folding pathways look like for  $\theta_0 = 1.39$ . Recall that  $\theta_0 = 1.39$  and  $x = 0.25$  were the parameters used in the preceding kinematic analysis, and that stable states, T1, T2, and T3, were indeed at  $\varphi = \pi/2$ ,  $\varphi = 3\pi/2$  and  $\varphi = \pi$ , as shown in Figure 4 (c), showcasing the predictive power of the inverse design. Figure 6 (b) demonstrates the impact of the alternative choice of  $\theta_0 = 2\pi - 1.39$ . Notice that T1 and T2 switch are now located on the right-hand path, while T3 now lies on the left-hand path. From this, we can conclude that if  $\theta_0 \in (0, \pi)$  [Eq. (18a)] then the two symmetric stable states will have  $\alpha \in (0, \pi)$ , whereas if we chose the  $\theta_0 \in (\pi, 2\pi)$  [Eq. (18b)] we will have that the two symmetric stable states have  $\alpha \in (\pi, 2\pi)$ .

## IX. CONCLUSION

We show via analysis and experiments a simplified technique of modeling Miura-Ori units with stretchable creases. Our analysis is based on a tractable model enabling the closed-form prediction of the stable state and folding paths of 4-vertex, non-Euclidean origami units with crease stretching. The derived model can accurately predict almost all of the observed behavior of a physical system. The model also enables an inverse design technique that gives two symmetric solutions for a desired shape. In theoretical terms, this is accomplished by connecting the disconnected regimes of non-Euclidean origami via crease stretching. This work provides an analytical model to access the design space of multistable origami, and lays the framework to allow for efficient inverse design of desired shapes based on accessible closed-form solutions the stability of which does not require ac-

tuation systems or facet deformation.

## X. ACKNOWLEDGEMENTS

We acknowledge funding from AB-Inbev and the Purdue Winkelman fellowship.

## XI. AUTHOR CONTRIBUTIONS

A.F.A and C.C.A. conceptualized the research, C.C.A conducted the model derivation, A.F.A. supervised the research, C.C.A and S.R. developed the experimental demonstrator, and A.F.A. and C.C.A prepared the manuscript.

- 
- [1] D. Melancon, A. E. Forte, L. M. Kamp, B. Gorissen, and K. Bertoldi, *Advanced Functional Materials* **32**, 2201891 (2022).
  - [2] P. Bhowad and S. Li, *Scientific Reports* **11**, 13002 (2021).
  - [3] E. Hawkes, B. An, N. M. Benbernou, H. Tanaka, S. Kim, E. D. Demaine, D. Rus, and R. J. Wood, *Proceedings of the National Academy of Sciences* **107**, 12441 (2010).
  - [4] S. Felton, M. Tolley, E. Demaine, D. Rus, and R. Wood, *Science* **345**, 644 (2014).
  - [5] M. Schenk and S. D. Guest, *Proceedings of the National Academy of Sciences* **110**, 3276 (2013).
  - [6] E. T. Filipov, T. Tachi, and G. H. Paulino, *Proceedings of the National Academy of Sciences* **112**, 12321 (2015).
  - [7] D.-Y. Lee, S.-R. Kim, J.-S. Kim, J.-J. Park, and K.-J. Cho, *Soft robotics* **4**, 163 (2017).
  - [8] L. H. Dudte, G. P. Choi, and L. Mahadevan, *Proceedings of the National Academy of Sciences* **118**, e2019241118 (2021).
  - [9] A. Walker and T. Stankovic, *Communications Materials* **3**, 4 (2022).
  - [10] Y. Zhao, Y. Wei, Y. Jia, S. Li, M. Zhang, L. Zeng, Y. Yang, and J. Mitani, *Journal of Computational Design and Engineering* **9**, 1498 (2022).
  - [11] K. Xiao, Z. Liang, B. Zou, X. Zhou, and J. Ju, *Nature Communications* **13**, 7474 (2022).
  - [12] C. D. Santangelo, *Soft matter* **16**, 94 (2020).
  - [13] S. J. Callens and A. A. Zadpoor, *Materials Today* **21**, 241 (2018).
  - [14] V. Brunck, F. Lechenault, A. Reid, and M. Adda-Bedia, *Physical Review E* **93**, 033005 (2016).
  - [15] E. A. Peraza-Hernandez, D. J. Hartl, R. J. Malak Jr, and D. C. Lagoudas, *Smart Materials and Structures* **23**, 094001 (2014).
  - [16] J. L. Silverberg, J.-H. Na, A. A. Evans, B. Liu, T. C. Hull, C. D. Santangelo, R. J. Lang, R. C. Hayward, and I. Cohen, *Nature materials* **14**, 389 (2015).
  - [17] C. Liu and S. M. Felton, *Physical review letters* **121**, 254101 (2018).
  - [18] K. Liu, T. Tachi, and G. H. Paulino, *Nature communications* **10**, 4238 (2019).
  - [19] S.-M. Baek, S. Yim, S.-H. Chae, D.-Y. Lee, and K.-J. Cho, *Science Robotics* **5**, eaaz6262 (2020).
  - [20] B. H. Hanna, J. M. Lund, R. J. Lang, S. P. Magleby, and L. L. Howell, *Smart Materials and Structures* **23**, 094009 (2014).
  - [21] B. Sargent, J. Butler, K. Seymour, D. Bailey, B. Jensen, S. Magleby, and L. Howell, *Journal of Mechanisms and Robotics* **12** (2020).
  - [22] H. Fang, S. Li, H. Ji, and K. Wang, *Physical Review E* **95**, 052211 (2017).
  - [23] S. Waitukaitis, R. Menaut, B. G.-g. Chen, and M. Van Hecke, *Physical review letters* **114**, 055503 (2015).
  - [24] B. G.-g. Chen and C. D. Santangelo, *Physical Review X* **8**, 011034 (2018).
  - [25] S. Waitukaitis and M. Van Hecke, *Physical Review E* **93**, 023003 (2016).
  - [26] M. Stern, V. Jayaram, and A. Murugan, *Nature communications* **9**, 4303 (2018).
  - [27] T. Tachi and T. C. Hull, *Journal of Mechanisms and Robotics* **9**, 021008 (2017).
  - [28] M. Berry, M. Lee-Trimble, and C. Santangelo, *Physical Review E* **101**, 043003 (2020).
  - [29] S. Waitukaitis, P. Dieleman, and M. van Hecke, *Physical Review E* **102**, 031001 (2020).
  - [30] K. A. Seffen, *Physical Review E* **94**, 013002 (2016).
  - [31] J. McInerney, B. G.-g. Chen, L. Theran, C. D. Santangelo, and D. Z. Rocklin, *Proceedings of the National Academy of Sciences* **117**, 30252 (2020).
  - [32] R. Foschi, T. C. Hull, and J. S. Ku, *Physical Review E* **106**, 055001 (2022).
  - [33] K. Liu, P. P. Pratapa, D. Misseroni, T. Tachi, and G. H. Paulino, *Advanced Materials* **34**, 2107998 (2022).
  - [34] K. Liu, T. Tachi, and G. H. Paulino, *Journal of Applied Mechanics* **88** (2021), 10.1115/1.4050556, 091002, [https://asmigitalcollection.asme.org/appliedmechanics/article-pdf/88/9/091002/6697121/jam.88.9\\_091002.pdf](https://asmigitalcollection.asme.org/appliedmechanics/article-pdf/88/9/091002/6697121/jam.88.9_091002.pdf).
  - [35] B. Liu, J. L. Silverberg, A. A. Evans, C. D. Santangelo, R. J. Lang, T. C. Hull, and I. Cohen, *Nature Physics* **14**, 811 (2018).



- [36] L. Huang, P. Zeng, L. Yin, B. Liu, Y. Yang, and J. Huang, *Mechanism and Machine Theory* **174**, 104886 (2022).
- [37] F. Haas, *Geometry and mechanics of hind-wing folding in Dermaptera and Coleoptera*, Ph.D. thesis, Exeter University, Biological Sciences Department (1994).
- [38] H. Rajabi, N. Ghoroubi, K. Stamm, E. Appel, and S. Gorb, *Acta Biomaterialia* **60**, 330 (2017).
- [39] A. M. Mountcastle and S. A. Combes, *Journal of Experimental Biology* **217**, 1108 (2014).
- [40] S. N. Gorb, *Naturwissenschaften* **86**, 552 (1999).
- [41] Z. Song, Y. Yan, J. Tong, and J. Sun, *Journal of Materials Science* **55**, 4524 (2020).
- [42] F. Haas, S. Gorb, and R. Blickhan, *Proceedings of the Royal Society of London. Series B: Biological Sciences* **267**, 1375 (2000).
- [43] K. Saito, S. Yamamoto, M. Maruyama, and Y. Okabe, *Proceedings of the National Academy of Sciences* **111**, 16349 (2014).
- [44] F. Haas, S. Gorb, and R. Wootton, *Arthropod Structure & Development* **29**, 137 (2000).
- [45] J. A. Faber, A. F. Arrieta, and A. R. Studart, *Science* **359**, 1386 (2018).
- [46] T. Jules, F. Lechenault, and M. Adda-Bedia, *Soft matter* **15**, 1619 (2019).
- [47] T. Jules, F. Lechenault, and M. Adda-Bedia, *Physical Review E* **102**, 033005 (2020).
- [48] B. Y. Dharmadasa and F. Lopez Jimenez, in *AIAA Scitech 2021 Forum* (2021) p. 1258.
- [49] M. Gori and F. Bosi, *Extreme Mechanics Letters* **56**, 101849 (2022).
- [50] A. Iniguez-Rabago and J. T. Overvelde, *Extreme Mechanics Letters* **56**, 101881 (2022).
- [51] C. Huang, T. Tan, X. Hu, F. Yang, and Z. Yan, *Applied Physics Letters* **121**, 051902 (2022).
- [52] M. Lee-Trimble, J.-H. Kang, R. C. Hayward, and C. D. Santangelo, *Soft Matter* **18**, 6384 (2022).
- [53] H. Zhang, H. Feng, J.-L. Huang, and J. Paik, *Extreme Mechanics Letters* **45**, 101213 (2021).
- [54] Y. Feng, M. Wang, and X. Qiu, *International Journal of Solids and Structures* **241**, 111530 (2022).
- [55] P. Zhao, J. Liu, C. Wu, S. Ye, Q. Yang, and G. Hao, *International Journal of Mechanical Sciences* , 108444 (2023).
- [56] M. G. Walker and K. A. Seffen, *Thin-Walled Structures* **124**, 538 (2018).
- [57] W. Kim, J. Byun, J.-K. Kim, W.-Y. Choi, K. Jakobsen, J. Jakobsen, D.-Y. Lee, and K.-J. Cho, *Science robotics* **4**, eaay3493 (2019).
- [58] H. Rajabi, S. H. Eraghi, A. Khaheshi, A. Toofani, C. Hunt, and R. J. Wootton, *Proceedings of the National Academy of Sciences* **119**, e2211861119 (2022).
- [59] S. Daynes, R. S. Trask, and P. M. Weaver, *Smart materials and structures* **23**, 125011 (2014).
- [60] S. Mintchev, J. Shintake, and D. Floreano, *Science Robotics* **3**, eaau0275 (2018).
- [61] F. Lechenault and M. Adda-Bedia, *Physical review letters* **115**, 235501 (2015).
- [62] T. Yu, *International Journal of Solids and Structures* **246**, 111588 (2022).
- [63] M. Walker, *Physical Review E* **101**, 043001 (2020).
- [64] S. Rojas, D. M. Boston, and A. F. Arrieta, in *Bioinspiration, Biomimetics, and Bioreplication IX*, Vol. 10965 (SPIE, 2019) pp. 134–142.
- [65] S. Rojas, K. S. Riley, and A. F. Arrieta, *Journal of the Royal Society Interface* **19**, 20220426 (2022).
- [66] M. Koryo, *The Institute of Space and Astronautical Science report* **618**, 1 (1985).
- [67] Y. Li and S. Pellegrino, *Journal of the Mechanics and Physics of Solids* **136**, 103772 (2020).
- [68] S. Kamrava, D. Mousanezhad, S. M. Felton, and A. Vaziri, *Advanced Materials Technologies* **3**, 1700276 (2018).